

## High-resolution crosswell imaging of a west Texas carbonate reservoir: Part 4 - Reflection imaging

Spyros K. Lazaratos\*, Jerry M. Harris†, James W. Rector III\*\*, and Mark Van Schaack‡

### ABSTRACT

Reliable crosswell reflection imaging is a challenging task, even after the data have been wavefield-separated in the time domain. Residual, strong coherent noise is still present in the data. Stacking is complicated by the wide range of reflection incidence angles available for imaging. With wavelengths of a few feet, small misalignments as a result of velocity or geometric errors produce destructive interference and degrade the quality of the stacked image. We present an imaging sequence that addressed these complications and allowed us to produce high-quality stacked images for both P- and S-waves from a large-volume crosswell data set. A very good tie was achieved at both wells. Heterogeneities imaged from well to well included very thin beds [less than 5 ft (1.5 m) thick] within the reservoir, pinchouts, and a major angular unconformity—the Grayburg/San Andres—that could not be observed reliably with any other technique (log correlation, surface seismic imaging, or tomography). In fact, the produced crosswell reflection images exhibit dramatically higher resolution and continuity than the P-wave traveltimes tomogram.

### INTRODUCTION

Several investigators (Baker and Harris, 1984; Beydoun et al., 1988; Khalil et al., 1993; Lazaratos, 1993) have pointed out the advantages of using reflections for crosswell imaging applications as opposed to conventional direct arrival traveltimes tomography. These advantages include:

- 1) imaging capability at and below the well TD, where the reservoir is often located,

- 2) improved vertical resolution over tomography, and
- 3) reduction of fundamental tomography imaging artifacts caused by aperture limitations and anisotropy.

However, there are many obstacles to overcome in producing an interpretable crosswell reflection image. Many of the obstacles are a result of the presence of coherent interference in crosswell seismic data. Arrivals other than reflections such as conversions, multiples, and borehole wave modes (e.g., tube waves) can obscure the desired primary reflections. Consequently, the problem of creating an interpretable crosswell reflection image generally cannot be satisfactorily addressed by simply mapping in depth (or migrating) and stacking the full-waveform data.

Although the brute stacks discussed by Rector et al. (this issue) show some continuous reflectors, there are obvious artifacts still remaining in the images. For example, both the P- and the S- brute stack reflection images contain steeply dipping (greater than 30°) features which are geologically impossible for this area. The brute stack results of Rector et al. (this issue) are somewhat disappointing given the fact that

- 1) the signal-to-noise ratio for this data set is excellent,
- 2) the well spacing is small (184 ft; practical applications might require crosswell surveys at well spacings larger than 1000 ft),
- 3) the trace spacing (2.5 ft) is smaller than what is usual for typical crosswell applications (5-10 ft), and
- 4) much of the prestack reflection data is highly coherent.

Causes of the brute stack degradation and a solution methodology are the subject of this paper. The process of improving upon the brute stacks was implemented after VSP-CDP mapping was applied to each gather in the eight wavefield-separated data subsets. The improvements to the brute stacks consisted of identifying and attenuating coherent noise through angle transformation, muting, and band-

Manuscript received by the Editor March 17, 1994; revised manuscript received December 1, 1994.

\*Formerly Department of Geophysics, Stanford University; currently TomoSeis, Inc., 1650 W. Sam Houston Pkwy N., Houston, TX 77043.

†Department of Geophysics, Stanford University, Stanford, CA 94305.

\*\*Engineering Geoscience, University of California at Berkeley, Berkeley, CA 94720.

© 1995 Society of Exploration Geophysicists. All rights reserved.

pass filtering, and enhancement of stack quality through residual alignment statics. The latter process is similar to residual statics corrections in conventional surface seismic data processing.

#### EVENT IDENTIFICATION AND COHERENT NOISE ATTENUATION

To improve the brute stacks, it was important to develop ways of visualizing the data and gaining a physical understanding of the types of noise remaining after wavefield separation. In this section we introduce different postmap [reflection mapping was formulated using a modified VSP-CDP transform, Wyatt and Wyatt (1981)] sorting domains, we explore the characteristics of reflected signal and noise in these domains, and we discuss techniques by which the residual noise can be attenuated after mapping.

#### Mapped common-source/receiver gathers

Unlike the examples shown by Rector et al. (this issue) where we focused our discussion on S-to-S reflections, we will examine the mapped gathers for both P-to-P and S-to-S reflections. Figure 1a shows a common-source gather from a depth of 2930 ft after wavefield separation to enhance P-downgoing reflections, and Figure 2a shows the same gather after mapping. A common element in the appearance of most crosswell reflection gathers and, in fact, of most VSP reflections is the high coherency of the reflections near the direct arrival. As we move inside the wavefield along a reflection event, we reach a zone around the shear direct arrival (labeled shear-noise barrier on Figures 1a and 2a) where the event often gets lost in other events. Comparison of raw and processed data reveals that these other events are S-to-S reflections or S-to-P converted reflections that have moveouts similar to the P-to-P reflections. Because the moveout of these coherent noise arrivals is similar to the P-to-P reflections, they were not removed by the wavefield separation processing.

Figures 1b and 2b show the same common-source gather and the equivalent mapped gather after processing aimed at enhancing downgoing S-reflections. Comparing Figures 1 and 2, we see that the noise affecting S-reflections is of a different nature than the noise affecting the P-reflections. Most elastic modes that were a source of noise for the P-wave reflections-direct S, transmitted conversion (P-to-S and S-to-P) and P-to-S reflected conversions-arrive earlier than the S-to-S reflections and do not interfere with them.

In the mapped gathers, the coherent noise dips from left to right for the P-reflections, while for the S-reflections it dips from right to left. This happens because in the time-domain premap data, the coherent modes that represent the most significant noise components for the P-reflections have moveouts smaller than the moveout of the P-to-P reflections; while for S-reflections, the noise has a moveout larger than that of the S-to-S reflections. We interpret the residual large-moveout noise in the mapped S-reflection data to be residual tube waves. For this data set, the tube wave was the only arrival with a moveout greater than that of the S-to-S reflections, and for higher frequencies, the tube wave was

spatially aliased and could not be effectively separated from the S-to-S reflections.

#### Common-reflection-point gathers

Another important type of gather is formed by extracting out of every mapped common-source or common-receiver gather the trace that corresponds to a particular horizontal position between the wells. The gathers that are produced in this fashion are called common-reflection-point gathers. Using the surface seismic analogy, we can think of these gathers as NMO-corrected common-midpoint gathers. A common-reflection-point gather for downgoing P-reflections is shown in Figure 3a. Every trace in the gather comes from

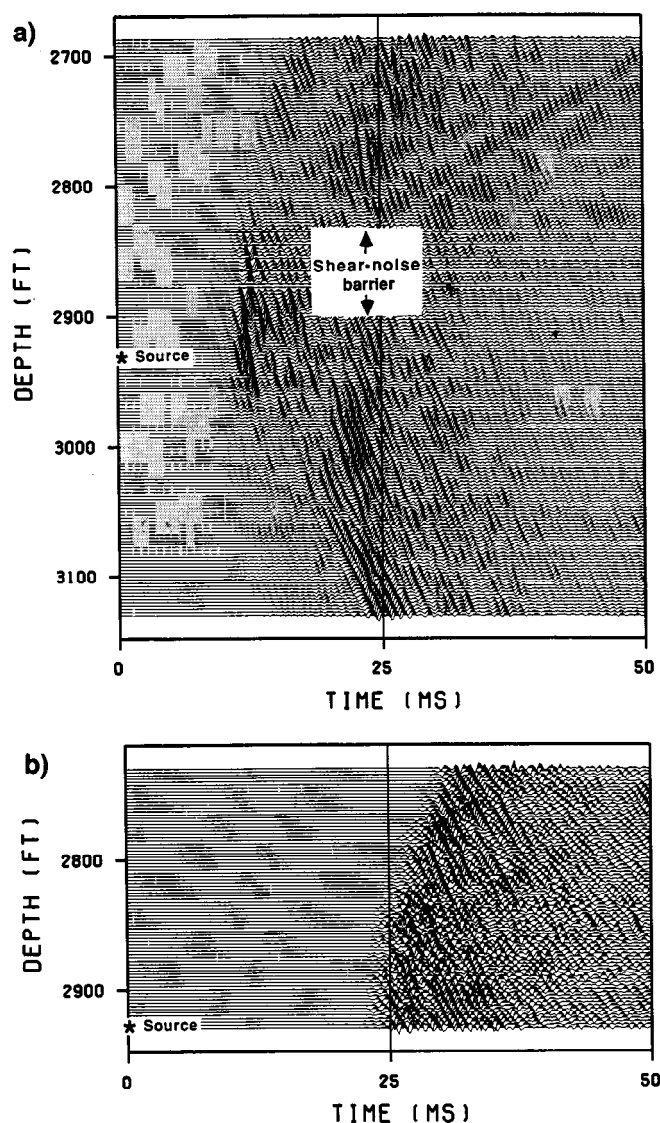


FIG. 1. (a) Common source gather [source depth = 2930 ft (895 m)] after wavefield-separation processing aimed at enhancing P-to-P downgoing reflections. (b) Common source gather after wavefield-separation processing aimed at enhancing S-to-S downgoing reflections.

a different mapped common-receiver gather. The number of traces gives the fold.

The quality of both the P-to-P and S-to-S common-reflection-point gathers for this data set deteriorated dramatically as the reflection point moved horizontally toward the middle of the interwell region. We believe that this is, in part, a result of the wavefield separation techniques used in Rector et al. (1995, this issue), which were optimized for reflections coming from horizontal positions near the wells. Figures 3b and 3c show common-reflection-point gathers for a distance 50 ft (15 m) (approximately 1/4 the well-to-well distance) and 90 ft (27 m) (approximately 1/2 the well-to-well distance) from the source well, respectively. Notice the decrease in the coherency of the gathers in Figure 3c. With

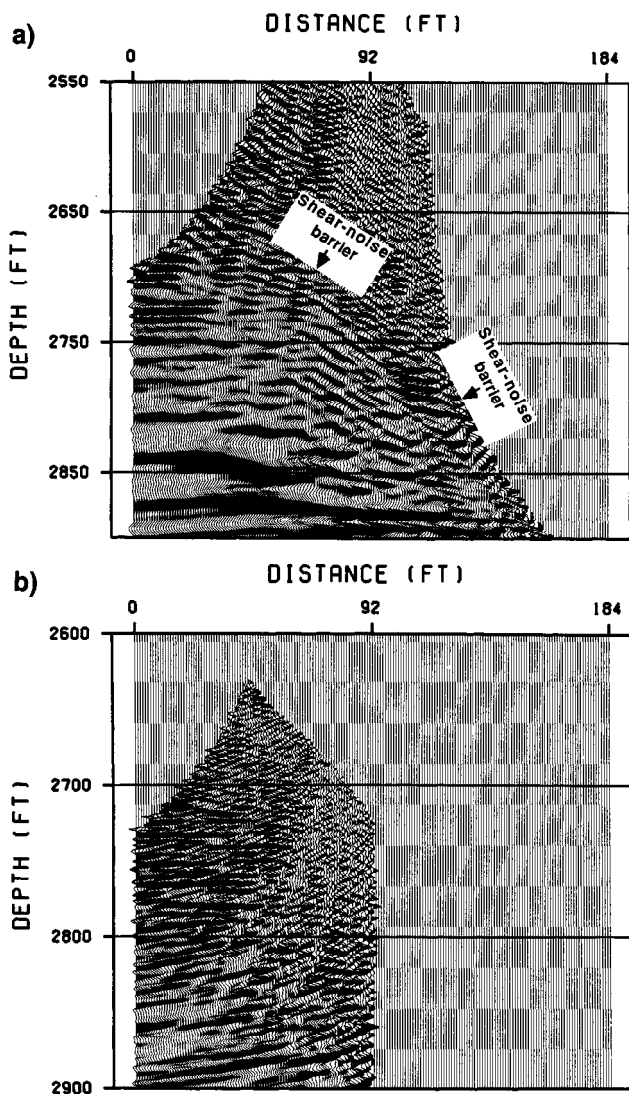


FIG. 2. (a) VSP-CDP mapped common source gather [source depth = 2930 ft (895 m)] of Figure 1a using tomogram-derived 1-D P-wave velocity model shown in Figure 11 of Rector et al. (1995, this issue). (b) VSP-CDP mapped common source gather of Figure 1b using S-wave velocity model shown in Figure 11 of Rector et al. (1995, this issue).

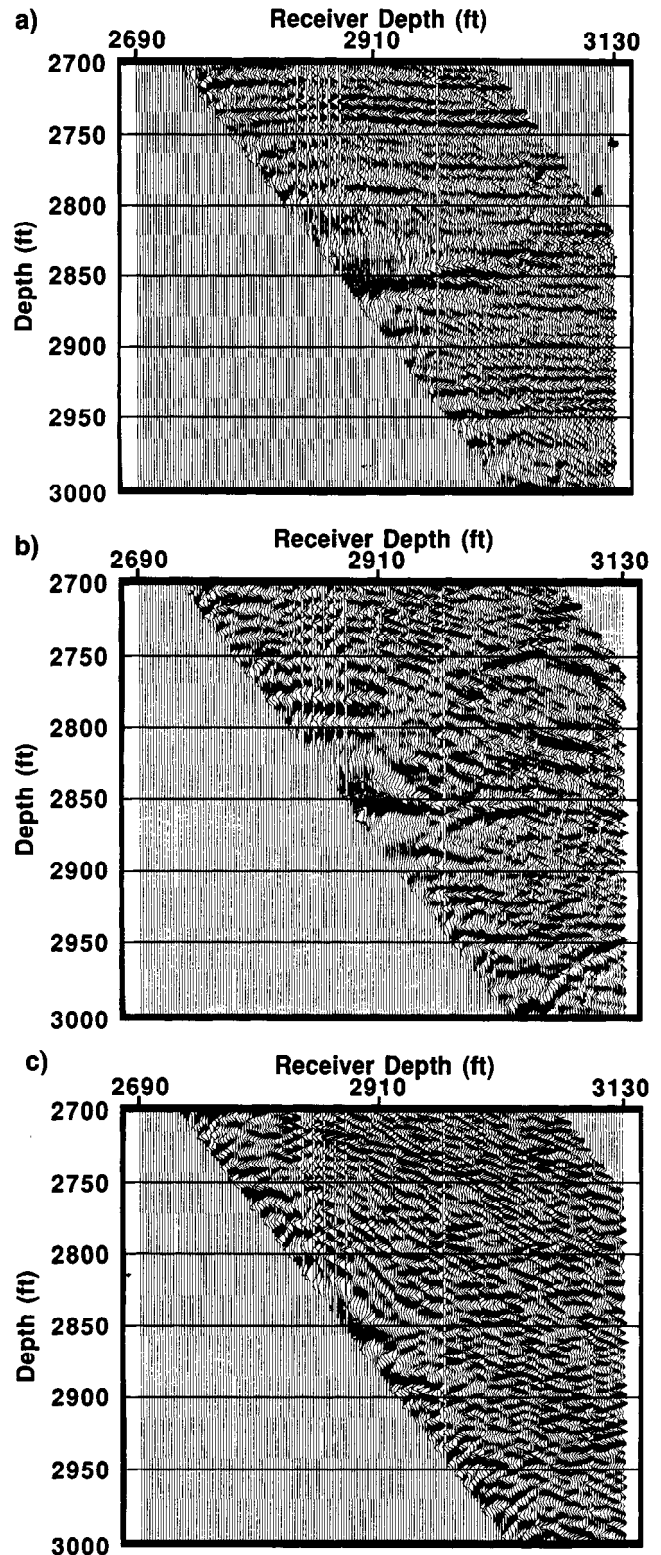


FIG. 3. (a) Common-reflection-point gather for the downgoing P-reflections. The reflection point is 10 ft (3 m) from the source well. (b) Same as (a) except that the reflection point is 50 ft (15 m), from the source well. (c) Same as (a) except that the reflection point is 90 ft (27 m) from the source well (approximately midway between the source and receiver wells).

the data in Figure 3c, it would be very difficult to obtain reliable statics and velocity information.

#### Incidence-angle transformation

Common-source and common-receiver gathers, although naturally produced during data acquisition, have little physical meaning. A more meaningful and useful way to examine the data is to transform the common-reflection-point gathers into constant-incidence-angle sections, defined by the incidence-angle transformation. This transformation is shown in Figure 4. Consider a gather from a common reflection point at a distance  $X$  from the source well. Under the assumption of straight rays and a horizontal reflector, the source depth  $Z_s$  is given by

$$Z_s = Z - X/\tan \phi, \quad (1)$$

where  $Z$  is the reflector depth and  $\phi$  is the incidence angle measured with respect to the vertical.

The transformation to the incidence-angle domain simply amounts to finding the data sample with coordinates  $(Z_s, Z)$  and mapping it to the new coordinates  $(\phi, Z)$ , where the old and new coordinates are related by equation (1). The implementation used for the data in this study assumed straight rays and horizontal reflectors. The new gathers produced by this transformation are termed *Amplitude-versus-Angle (AVA) gathers*, to distinguish them from common-reflection-point gathers. An example of the transformation applied to the data in Figure 3 is shown in Figure 5. The character of the AVA gathers is not fundamentally different from the character of common-reflection-point gathers.

Following the incidence-angle transformation, we can form sections for which the incidence angle is constant for all

reflection points. We call them *constant-angle sections*. For a constant-velocity medium and horizontal reflectors, the reflection traveltime  $t$  is given by:

$$t = X_{well}/V \sin \phi, \quad (2)$$

where  $X_{well}$  is the well-to-well distance, and  $V$  is the velocity. Thus, for a constant-angle section, the reflection traveltimes are constant and constant-angle sections are related to time slices of the data cube. In fact, for a constant-velocity medium, the common-angle domain is conceptually identical to the common-midpoint domain described in Rector et al. (1994).

The constant-angle sections are very useful for event identification and noise elimination, and in many respects are superior to common-source or common-receiver gathers. Many parameters of the mapped reflected wavelet, including wavelet stretch, radiated and received amplitude, geometric spreading, reflection coefficient, velocity sensitivity, and lateral resolution, are more or less constant for a given incidence angle. In a mapped common-source/receiver gather all of the aforementioned parameters vary as a function of position because the incidence angle is depth and offset dependent.

Residual coherent noise in the mapped gathers is also angle dependent. According to equations (1) and (2), constant-time lines in premapped gathers map to lines which form an angle with the vertical equal to the incidence angle. So, zero-moveout events in premapped data will appear as linear dipping events in constant-angle sections. For large incidence angles the dip will be small, for more vertical incidence angles the dip will be larger. Consequently, mul-

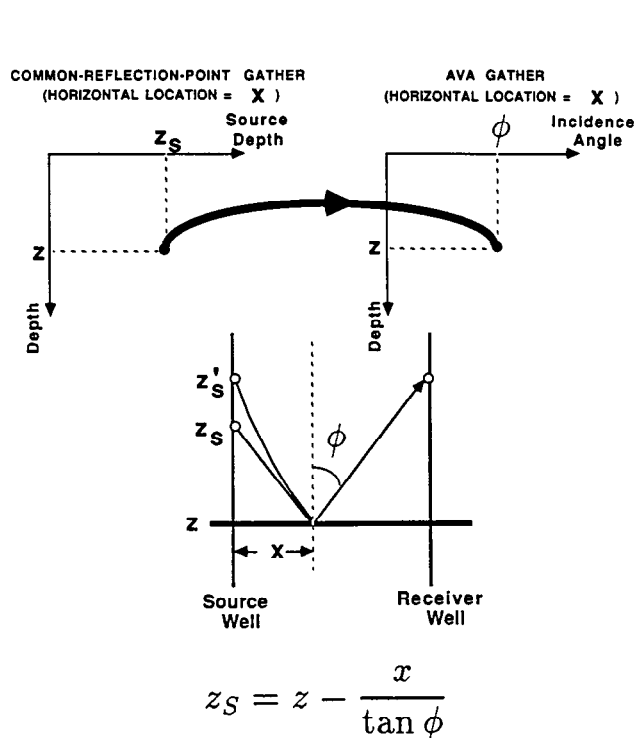


FIG. 4. Transformation of the mapped data cube from source/receiver depth to incidence angle.

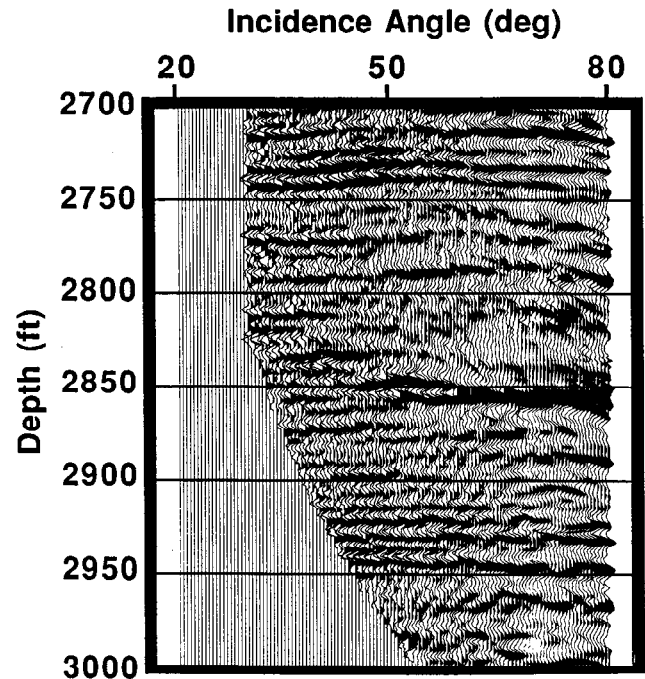
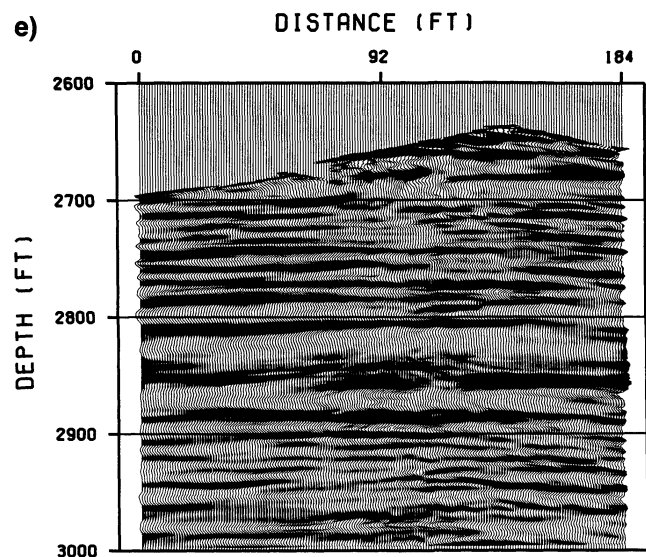
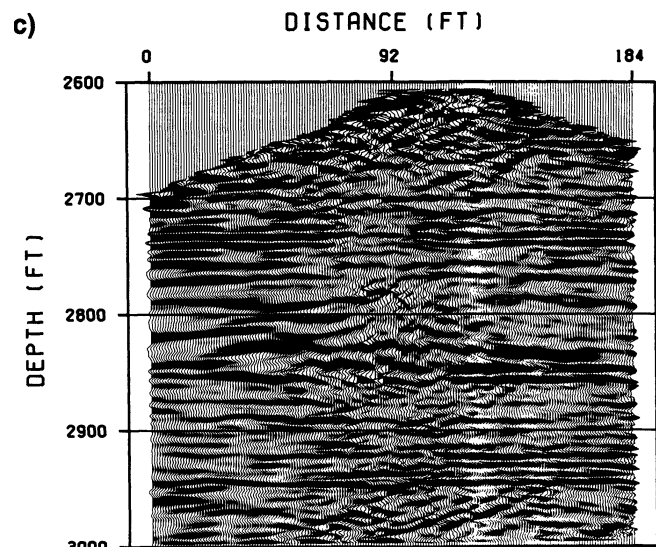
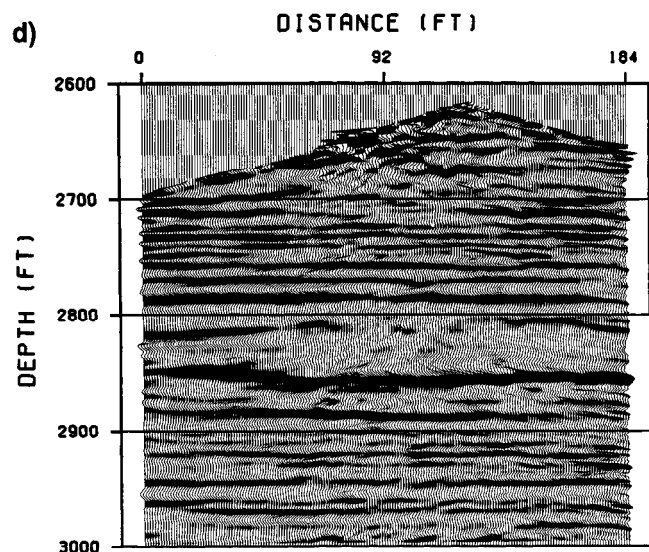
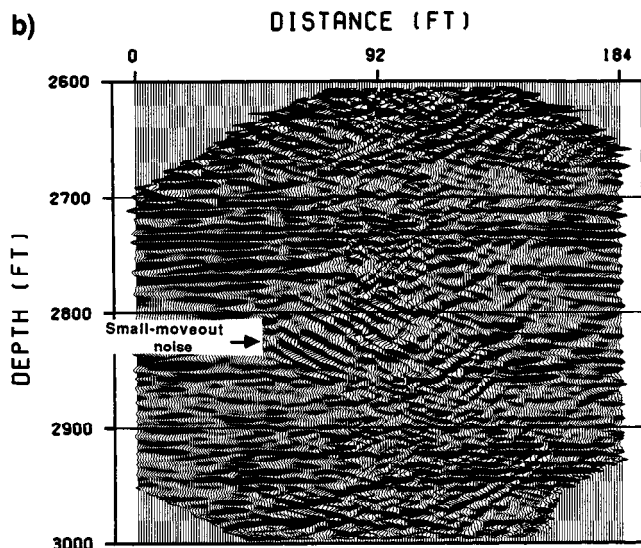
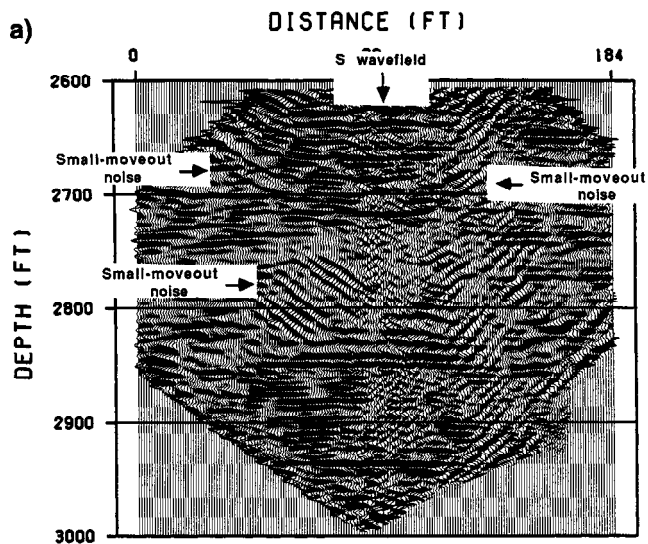


FIG. 5. Amplitude-versus-angle (AVA) gather for the P-downgoing reflections corresponding to the common-reflection-point gather shown in Figure 3a. The reflection point is 10 ft (3 m) from the source well.

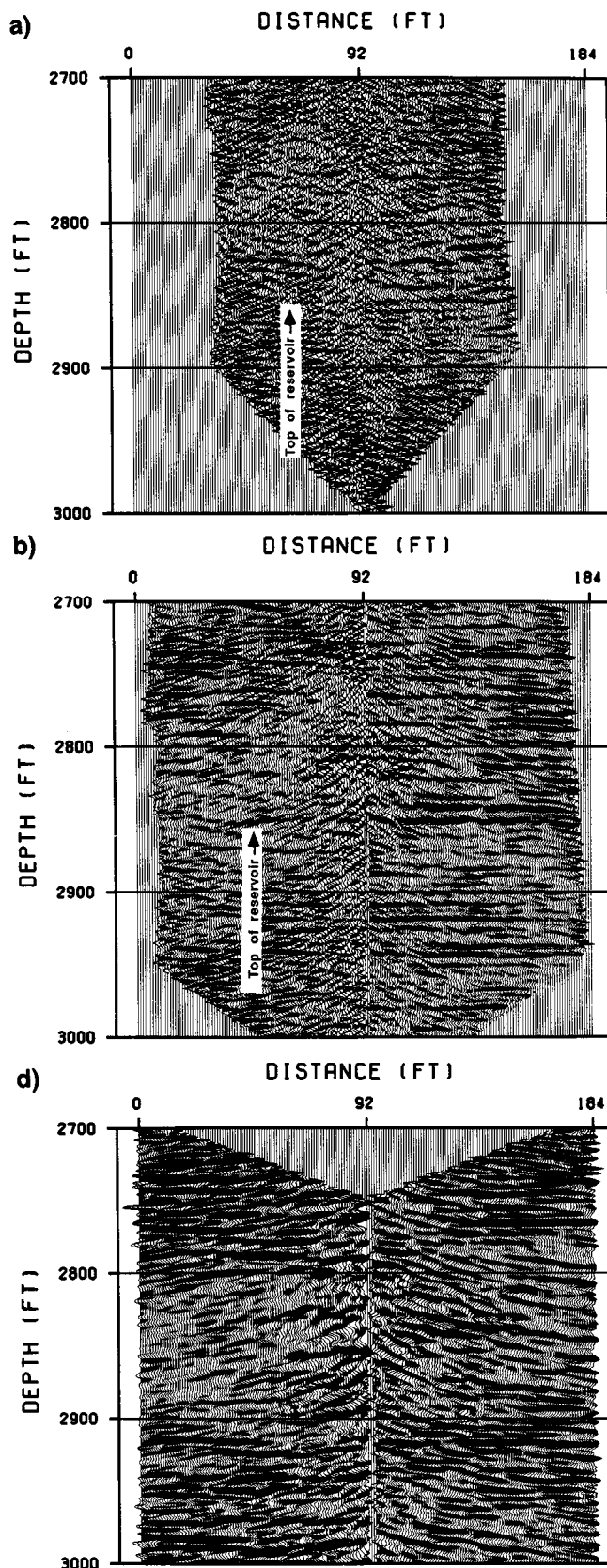


tichannel dip filters should be configured to be angle dependent-becoming more surgical (narrower passband) at wider incidence angles. Angle-dependent multichannel filtering would also insure that the more drastic filters needed for wavefield separation at wider incidence angles would not unnecessarily reduce the higher lateral resolution potentially achievable with the smaller incidence angles. Although incidence-angle dependent filtering was not used on this data set, this filtering domain holds promise for developing improvements to the wavefield separation techniques used in Rector et al. (this issue).

#### Constant-angle sections-Examples

Figure 6 shows constant-angle sections corresponding to incidence angles between 30° and 70° for P-downgoing reflections. Notice that, as predicted by theory (Lazaratos, 1993), the depth wavelet becomes broader as the angle of

FIG. 6. Constant incidence angle sections for P-downgoing reflections. (a) 30°, (b) 40°, (c) 50°, (d) 60°, (e) 70°.



incidence increases but remains approximately constant for the same depth and angle of incidence. This makes constant-angle sections very useful for event identification. It is easier to identify continuous events in this unstacked display than in the brute stack, suggesting that there are significant improvements to the signal-to-noise ratio that can be made in the final stack. The ability to identify continuous events in some of the constant angle sections also means that statics and velocity analysis could be performed in this domain.

The strong, steeply dipping noise observed on the 30° and 40° sections marks the boundary where the P-reflections start entering the direct S-wavefield. We should be extremely cautious when interpreting events in this zone as horizontal events may be downgoing S-to-S reflections or S-to-P converted reflections. In producing the final P-to-P reflection stack we chose to mute out the higher incidence angles in the center of the image to avoid the contribution of these "interference" reflections.

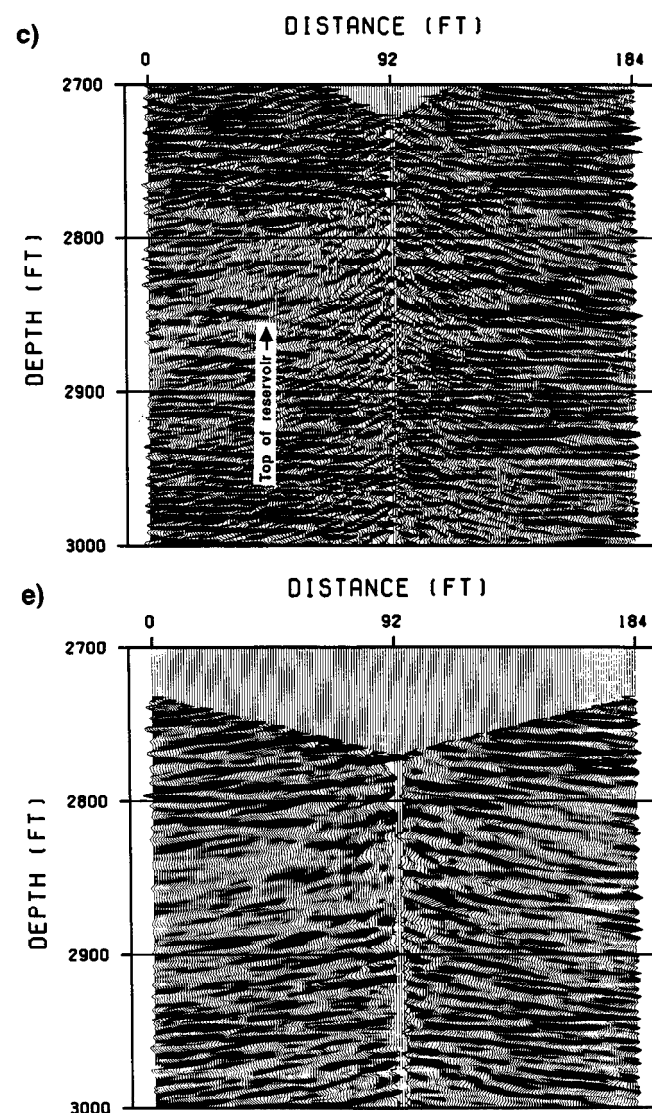


FIG. 7. Constant-incidence-angle sections for S-downgoing reflections. (a) 30°, (b) 40°, (c) 50°, (d) 60°, (e) 70°.



Figure 7 shows the same constant-angle sections for the S-downgoing reflections. The 30°, 60°, and 70° sections are dominated by tube wave noise. Such gathers were eliminated from the final stack. We obtain the best signal-to-noise ratio for S-reflections between 35° and 55°, as we would expect, given the radiation pattern of the shear waves (Van Schaack et al., 1992). Notice that the top of the reservoir [at about 2850 ft (871 m)] is visible only near the middle for the 40° section.

### Wavenumber filtering

Event identification on very wide-angle reflection sections can often be difficult. One reason is the possible existence of phase shifts associated with postcritical reflections. Perhaps more troublesome though are the effects of wavelet stretch after VSP-CDP mapping. In Lazaratos (1993) it is shown that, for a constant mapping velocity  $V$ , the mapped wavelength  $\lambda_m$  is related to the premapped temporal frequency  $f$  through:

$$\lambda_m = V/2f \cos \phi, \quad (3)$$

where  $\phi$  is the reflection angle of incidence (measured from the vertical). As the incidence angle increases, the mapped wavelengths get larger and the energy in the vertical wavenumber spectrum moves toward the smaller wavenumbers. Wavelet stretch makes it difficult to compare mapped data corresponding to significantly different incidence angles. One solution to this problem is to perform wavenumber band-pass filtering to a common band. Figure 8 shows the

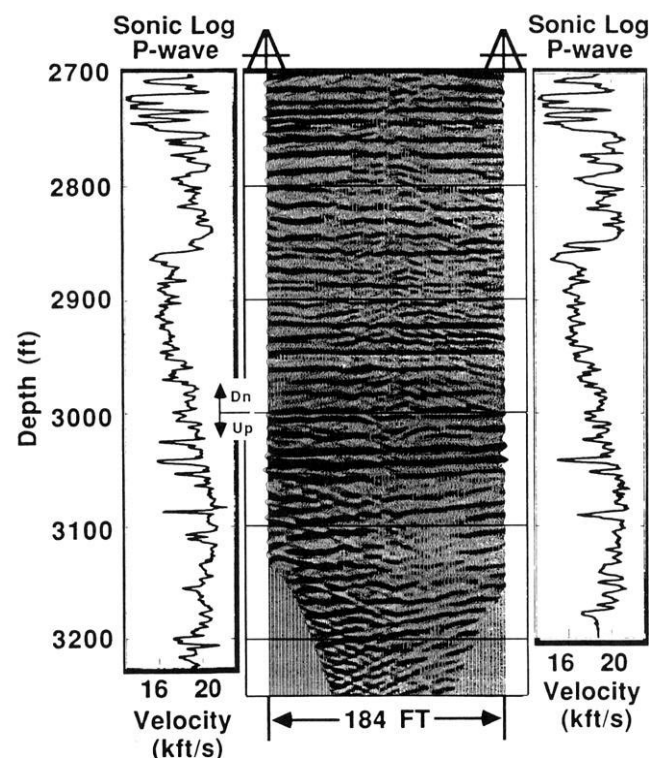


FIG. 8. Brute stack *P-to-P* reflections after wavenumber filtering to attenuate very low wavenumber (predominantly) wide angle reflections.

*P-to-P* reflection section after wavenumber filtering to a common band--attenuating very low wavenumber (wide angle) components. The principal improvement in the image over the brute stack is the elimination of low-wavenumber noise from the wavelength-filtered image. In Figure 12 of Rector et al. (this issue) there are two strong events close to the receiver well, one at 2810 ft (859 m) dipping slightly from right to left, the other at about 3130 ft (956 m), dipping slightly from left to right. These are both interpreted to be low-wavenumber, low-dip, coherent-noise-generated artifacts. In the wavenumber-filtered image (Figure 8) these artifacts are attenuated.

### IMPERFECT ALIGNMENT OF EVENTS AND RESIDUAL MOVEOUT CORRECTIONS

#### The problem

Even after coherent noise attenuation through the techniques discussed in the last section, the stacked output was not particularly of good quality. In surface seismic imaging, it is crucial that the NMO-correct data are aligned to within 1/4 wavelength. Likewise, in crosswell mapped data, event misalignments of more than 1/4 the dominant wavelength will produce significant degradation of the stacked section. For this dataset, typical wavelengths are of the order of 10 ft (3 m) for *P*-waves and 5 ft (1.5 m) for *S*-waves. Very small misalignments of under 2 ft (0.6 m) could have a significant detrimental effect on the quality of the final stack--particularly for the *S*-wave stack. In fact, the inferiority of the *S*-wave stack as compared to the *P*-wave stack could be primarily attributable to reflection misalignment, since the prestack data were of higher quality for *S*-waves, and angle and wavenumber filtering had very little impact on the *S*-wave stack.

Misalignments on the order of 2 ft (0.6 m) for the mapped data can be produced easily by a number of factors including: incorrect velocity model used for mapping, in-plane and out-of-plane dips, velocity anisotropy, and source/receiver location and/or timing errors. Lazaratos (1993) pointed out that the misalignment problem becomes worse as the ratio of the well-to-well distance to the wavelength increases. An example of imperfect alignment for the *P*-downgoing waves is shown in the AVA gather of Figure 5 (the *S*-downgoing waves were even worse). If the velocity model and source/receiver locations were correct, the reflection events in these gathers should be flat and independent of reflector dip. Yet, for the gather shown in Figure 5, the events have curvature, particularly for the depth range from 2700 to 2800 ft (825 m to 856 m). Obviously, for this data set, the tomogram velocities are not optimal for reflection imaging. Similar results have been observed with other data sets imaged with tomogram-derived velocities.

#### The solution-residual moveout corrections

The problem of event misalignment actually consists of two parts:

- 1) Misalignment of events degrades the quality of the stack.

- 2) Misalignment of events means that the velocity model is incorrect, which implies that the events are mapped to incorrect depths and lateral locations.

The solution proposed here addresses only the first part. Time-to-depth conversion in crosswell reflection data is less of a problem than time-to-depth conversion in surface seismic data because the reflection depth at the wells is known.

In surface seismic analysis, coherency improvements to the brute stack are produced by statics and velocity analysis. Velocity analysis for crosswell data and an approximation analogous to the rms velocity of surface seismic has not yet been derived. One difficulty in deriving such a relationship is the wide-angle nature of crosswell reflection data. Crosswell raypaths corresponding to the same reflection point may not cross the same layers—for very wide angles, the reflection raypaths may remain in the same layer, while for more vertical incidence angles, the raypaths may cross a number of different layers.

In the residual moveout corrections applied to this data set, reflection events in AVA gathers were interactively picked to produce residual corrections that will align the reflection events as shown in Figure 9. The events are aligned to a reference angle. Figure 9 shows the AVA gather in Figure 5 aligned to the 80° incidence angle. The choice of a reference angle, to which events are aligned, is arbitrary. Aligning the events at any angle solves the problem of stack degradation as a result of event misalignment; yet, uncertainty in depth positioning is still present after the corrections. The residual-moveout corrections applied to this data set were never larger than a wavelength, because of the good initial velocity model provided by the tomogram, so the depth uncertainty for the reflectors is about this order of

magnitude. If the velocity model were significantly wrong, iterative velocity analysis and residual-moveout corrections (similar to the iterative velocity analysis and statics procedure in surface seismic) would be required. However, one would expect that the tomogram-derived velocities are generally adequate and will remove the need for iterative techniques such as reflection tomography (Bishop et al., 1985; Stork, 1988).

#### THE IMAGING SEQUENCE AND FINAL STACKS

The principles and ideas described in the last two sections form the building blocks of the imaging sequence used on this data set. As described in (Rector et al. this issue), the eight wavefield-separated subsets were mapped using a 1-D velocity model derived from the P- and S-traveltime tomograms. A brute stack and a band-pass-filtered brute stack [Figure 12 in Rector et al. (this issue) and Figure 8] were then produced. The mapped common-source and common-receiver gathers were then angle-transformed, as described before, to produce data cubes for which one of the axes was incidence angle. The data cubes for mapped common-source and common-receiver gathers were then combined to produce constant-angle sections with well-to-well coverage. This step included interactive editing and selection of the best signal-to-noise ratio parts imaged with each of the two sorts. Then, for the case of P-wave imaging, the shear wave reflections, still present in the P-wavefield were muted. Mutes were picked interactively in constant-angle sections. The data were then moveout-filtered in common-angle sections and AVA gathers to further attenuate coherent noise. Partial stacks (stacks over a limited range of incidence angles) were then produced to further facilitate event identification. Then the range of angles over which the signal-to-noise ratio was optimal was selected. Extremely wide-angle reflections (larger than 65°) were muted to avoid problems associated with large wavelet stretch and postcritical reflections. Finally the data were dip- and wavenumber-filtered to a wavenumber band that was least contaminated by low-dip, low-wavenumber coherent noise.

At this stage the different gathers were compared for misalignment of events. Strong reflecting horizons were first picked. Then, based on the picked horizons, residual moveout corrections were applied. Before stacking, amplitude corrections were also applied. In this case the corrections included a straight-ray geometric spreading correction, and a radiation pattern correction based on a monopole source and receiver in a fluid-filled borehole (Lee and Balch, 1982; Schoenberg, 1986). The reason for making these corrections was not to attempt a detailed amplitude interpretation—the scaling performed in the wavefield separation and the strong effects of transmission and reflection on incidence angle make such corrections very complex—but rather to roughly equalize the contributions to the final stack of reflections recorded at different incidence angles. The P- and S- final stacks, along with synthetic seismograms derived from the acoustic logs, are shown in Figure 10. As with the brute stacks, the images from 2700 to 3000 ft (825 m to 929 m) were produced from downgoing reflections while the images below 3000 ft (929 m) were produced from upgoing reflections.

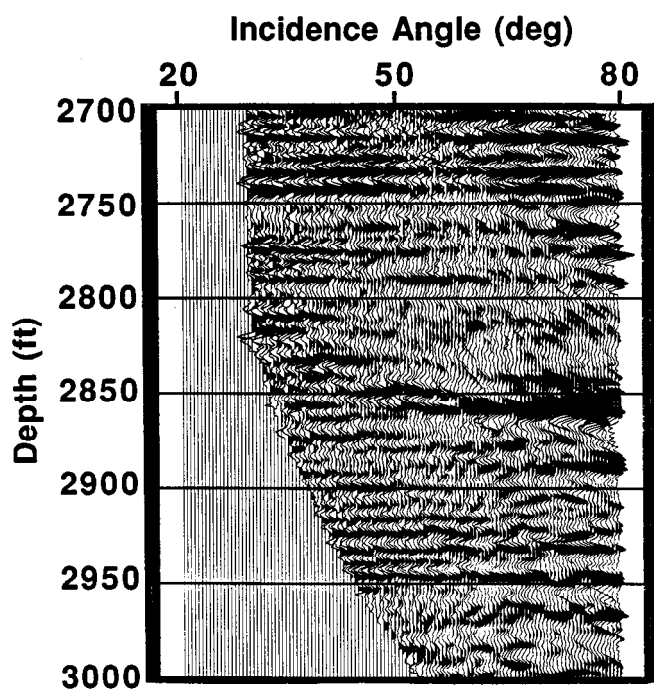


FIG. 9. AVA gather of Figure 5 after residual statics alignment to the 80° incidence angle event times.



The synthetics shown in Figure 10 were wavenumber-filtered versions of the sonic logs with a  $90^\circ$  phase shift to account for the phase difference between impedance and reflectivity. To make the synthetics compatible with the downgoing reflections, we reversed the polarity above 3000 ft (929 m). Obviously these synthetics are very qualitative and not really justifiable on an exact physical basis. Their only purpose is to help relate crosswell reflection events to the logs and guide the interpretation at the fre-

quency band of investigation. Normal-incidence synthetics would also be inexact. The only correct way to generate synthetics for this geometry would be to create a primaries-only synthetic data set, simulating the entire experiment (with radiation patterns and impedance effects), and process it in exactly the same way the real data were processed. Although a shear log was available only for the receiver well, comparisons showed that synthetics based on P-logs correlated well with shear synthetics.

Notice the good quality of both the *P*- and *S*-stacks, the excellent well tie with the synthetics, and the significant improvement that has been achieved over the brute stacks and the band-pass filtered stack. Perhaps the most prominent feature in the reflection images is an angular unconformity at a depth of 3050 ft (932 m). Below this depth the beds dip at approximately  $8^\circ$ . This unconformity, interpreted to be the interface between the carbonate San Andres and Grayburg formations, is shown in larger scale in Figures 11a and 11b. The unconformity, thought to be an important pressure-drive factor in many west Texas reservoirs, was not detected in any measurements (log, surface seismic, or tomography) made prior to the crosswell reflection images. In fact, visual sonic log correlations suggested no unconformity at all. Some interesting features can also be observed for the depth range from 2700 to 2800 ft (825 to 856 m) (Figures 12a and 12b). Both *P*- and *S*-images indicate horizontal bedding between 2700 and 2800 ft (825 and 856 m). Some prominent

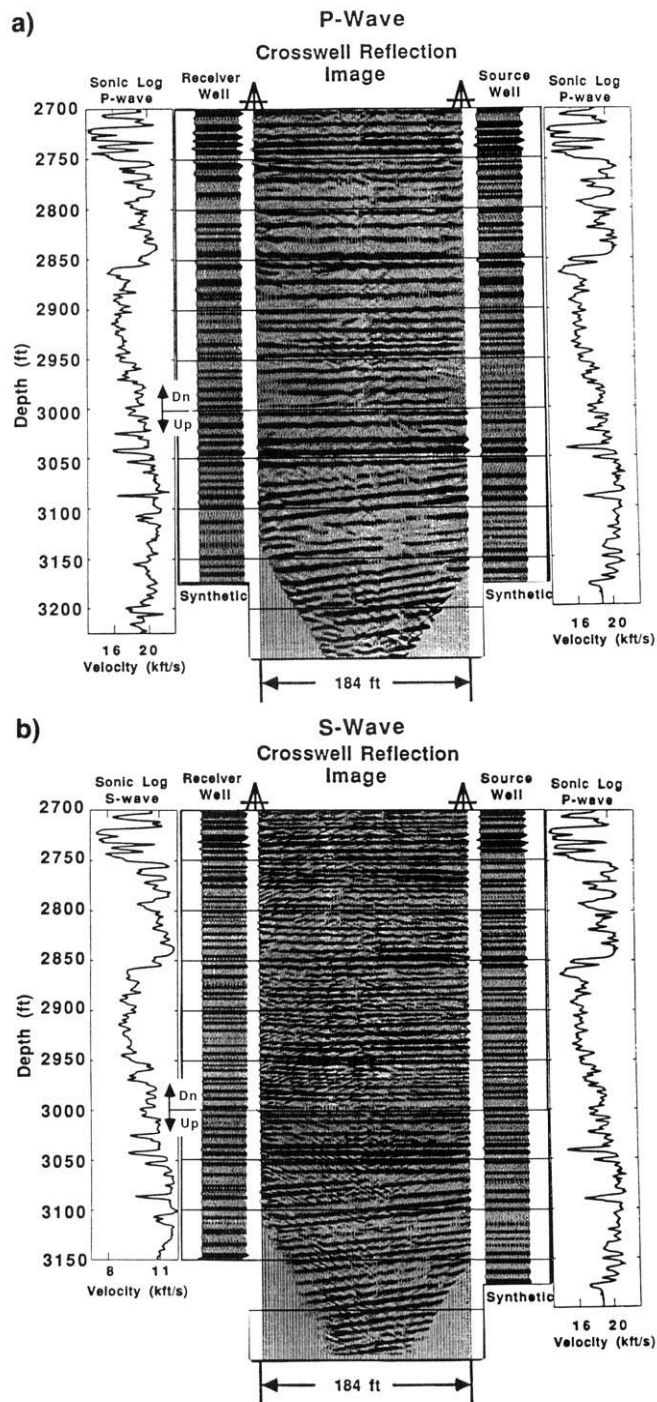


FIG. 10. (a) P-to-P and (b) S-to-S final stacks, sonic logs, and log-based synthetic seismograms.

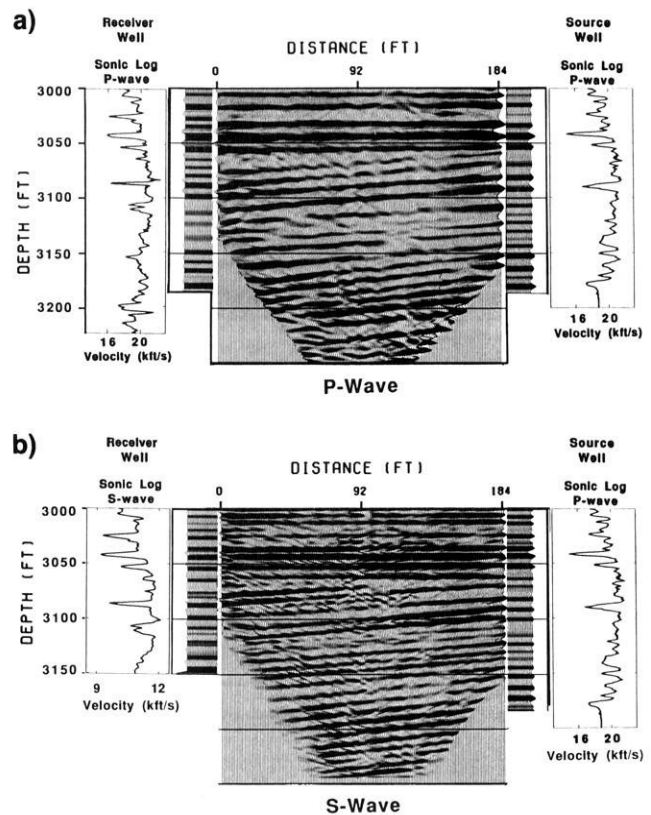


FIG. 11. (a) Larger scale depiction of *P-to-P* final stack isolating on the angular unconformity between the Grayburg and San Andres formations. (b) Same as (a) except *S-to-S* final stack.

reflectors in this zone are less than 5 ft thick. Below 2750 ft (840 m) we see lateral heterogeneity (also suggested by the logs) and on the S-wave image a pinchout can be seen.

Although the traveltome tomogram [Harris et al. (this issue)] successfully images the major layers, it offers significantly lower resolution than the reflection images. There is little evidence on the tomogram for the fine bedding inside the reservoir and the pinchout between 2750 and 2800 ft (840 and 856 m). Notice in particular that it would be hard to interpret the angular unconformity. This feature is very close to the bottom of the wells, where the tomogram suffers from coverage artifacts. The fact that the reflections can successfully image the area close to, or even below, the bottom of the wells is significant for reservoir characterization applications, since this is the area where the reservoir is most often located.

### CONCLUSIONS

Successful crosswell reflection imaging was achieved by a combination of two elements: premap wavefield separation [discussed in Rector et al. (this issue)] and an imaging sequence that consisted of postmap incidence-angle transformation and reflection-point-dependent angle muting, wavenumber filtering, and residual-moveout corrections. Wavefield separation followed by mapping (brute stack) failed to produce high-quality images. The poor quality of the

brute stack can be attributed to two causes. First, coherent noise was left over from the wavefield separation processing, obscuring reflections of interest. The characteristics of the coherent noise varied significantly as a function of reflection incidence angle. Second, reflection images produced from different gathers were not perfectly in phase, reducing the effectiveness of the stacking summation. The first difficulty was addressed by selecting for the final stacks the angles and wavenumbers least contaminated by noise. Constant-angle gathers were found to be an effective means for event identification and noise attenuation because of their stationary properties. The second difficulty was addressed by dynamic (depth-dependent) residual-moveout corrections.

The most important conclusion that can be drawn from this study is that crosswell reflection imaging is feasible and may become an important tool for high resolution reservoir imaging. For the first time, high resolution, high-quality crosswell reflection images were obtained showing important geologic features that could not be seen with surface seismic or with well log correlations.

### ACKNOWLEDGMENTS

The authors are grateful to the Gas Research Institute (GRI) and to the sponsors of the Seismic Tomography Project (STP) at Stanford University for supporting this work.

### REFERENCES

- 
- Baker, L. J., and Harris, J. M., 1984, Cross-borehole seismic imaging, Presented at the 54th Ann. Internat. Mtg. of SEG, Atlanta, Expanded Abstracts, 54.
- Beydoun, W. B., Delvaux, J., Mendes, M., Noual, G., and Tarantola, A., 1988, Practical aspects of an elastic migration/inversion of crosshole data for reservoir characterization: A Paris basin example: *Geophysics*, **54**, 1587-1595.
- Bishop T. N., Bube, K. P., Cutler, R. T., Langan, R. T., Love, P. L., Resnick, J. R., Shuey, R. T., Spindler, D. A., and Wyld, H. W., 1985, Tomographic determination of velocity and depth in laterally varying media: *Geophysics*, **50**, 903-923.
- Harris, J. M., Nolen-Hoeksema, R. C., Langan, R. T., Van Schaack, M., Lazaratos, S. K., Rector III, J. W., 1995, High-resolution crosswell imaging of a west Texas carbonate reservoir: Part 1-Project summary and interpretation: *Geophysics*, **60**, 667-681.
- Khalil, A. A., Stewart, R. R., Henley, D. C., 1993, Full-waveform processing and interpretation of kilohertz cross-well seismic data: *Geophysics*, **58**, 1248-1257.
- Lazaratos, S. K., 1993, Cross-well reflection imaging. Ph.D. Thesis. Stanford University.
- Lee, M. W., and Batch, A. H., 1982, Theoretical seismic wave propagation from a fluid-filled borehole: *Geophysics*, **47**, 1308-1314.
- Rector, I. W., Lazaratos, S. K., Harris, J. M., and Van Schaack, M., 1994, Multidomain analysis and wavefield separation of cross-well seismic data: *Geophysics*, **59**, 27-35.
- Rector J. W., Lazaratos S. K., Harris, J. M., and Van Schaack, M., 1995, High-resolution crosswell imaging of a west Texas carbonate reservoir: Part 3-Wavefield separation of reflections: *Geophysics*, **60**, 692-701.
- Schoenberg, M., 1986, Fluid and solid motion in the neighborhood of a fluid filled borehole due to the passage of a low-frequency elastic plane wave: *Geophysics*, **51**, 1191-1205.
- Stark, C., 1988, Ray trace tomographic velocity analysis of surface seismic reflection data, Ph.D. Thesis, California Institute of Technology.
- Van Schaack, M., Harris, J. M., Rector, J. W., and Lazaratos, S. K., 1992, High-resolution imaging of a west Texas carbonate reservoir: Part 2-Traveltime tomography, Presented at the 62nd Ann. Mtg. of SEG, New Orleans. Expanded Abstracts, 40-44.
- Wyatt, K. D., and Wyatt, S. B., 1981, Determination of subsurface structural information using the vertical seismic profile, Presented at the 51st Ann. Internat. Mtg. of SEG, 1915-1949.

FIG. 12. (a) Larger scale depiction of P-to-P final stack isolating on the 2700 to 2800 ft (825 to 856 m) interval showing horizontally continuous beds and a pinchout. (b) Same as (a) except S-to-S final stack. Since the S-wave-lengths are shorter, the short-wavelength pinchout can be seen better.